Controllable Synthesis and Morphology-Dependent Light Emission Efficiency of Zn2GeO4 Nanophosphors

Miguel Tinoco *, José Miguel Lendínez, José M Gonzalez-Calbet, Bianchi Méndez, Pedro Hidalgo *, Julio Ramírez-Castellanos

Posted Date: 11 September 2023

doi: 10.20944/preprints202309.0623.v1

Keywords: nanophosphors; Zn2GeO4; hydrothermal synthesis; luminescence

Article

Controllable Synthesis and Morphology-Dependent Light Emission Efficiency of Zn_2GeO_4 Nanophosphors

Miguel Tinoco [1,*], José Miguel Lendínez [2], José M. González-Calbet [1,3], Bianchi Méndez [2], Pedro Hidalgo [2,*] and Julio Ramírez-Castellanos [1]

[1] Departamento de Química Inorgánica, Facultad de Ciencias Químicas, Universidad Complutense de Madrid, Madrid, 28020, Spain
[2] Departamento de Física de Materiales, Facultad de Ciencias Físicas, Universidad Complutense de Madrid, Madrid, 28020, Spain
[3] ICTS National Center for Electron Microscopy, Universidad Complutense de Madrid, 28040 Madrid, Spain Madrid, 28020, Spain
* Correspondence: MT: mitinoco@ucm.es; Tel.: (+34)913948502; PH: phidalgo@ucm.es; Tel.: (+34)913944790

Abstract: Zn_2GeO_4 is considered a very promising alternative to current luminescent semiconductors. Previous results suggest that its emitted wavelength may depend on different variables, such as particle size and morphology, among others. In this work, we have prepared pure and highly homogeneous Zn_2GeO_4 nanorods under hydrothermal synthesis conditions with a willemite-like structure. Their luminescent properties have been explored and their band gap estimated, which are distinct to previously reported Zn_2GeO_4 bulk particles. Therefore, our results identify particle morphology as a crucial factor for maximizing and fine-tuning the luminesce of Zn_2GeO_4 nanophosphors.

Keywords: nanophosphors; Zn_2GeO_4; hydrothermal synthesis; luminescence

1. Introduction

III-V semiconductors are widely recognized as some of the most significant basic materials for the development of light-emitting devices worldwide, due to their exceptional capabilities.[1] Nevertheless, semiconductor industry is searching for novel light emitting materials due to the high toxicity of current semiconductors and some of their alternatives, especially those based on arsenic,[2] gallium,[3] or lead.[4] In addition, the production of indium, which is a common element appearing in III-V semiconductors, is highly dependent on the fluctuations of other metals markets as it is only obtained as a by-product of other metal ores processing.[5] Apart from that, rare earth elements, which appear in the composition of current phosphors, have been classified as critical raw materials by several international organizations, which have recommended lessening their usage in the industry.[6,7] All of these factors have intensified the search for novel semiconductor compounds, which may overcome most of these drawbacks.

Ternary oxides, particularly those based on ZnO and TiO_2, have emerged as some of the most promising candidates to replace current light-emitting semiconductors, fulfilling all previous requirements. Furthermore, various synthesis methods can be employed to prepare oxide nanophosphors with an up to standard purity and crystallinity with controlled morphologies and particle sizes, which can be easily tuned by simply modifying synthesis conditions.[8–11]

Among these materials, bulk Zn_2GeO_4 emits in the blue-green region, peaking at 2.39 eV. Nevertheless, its photoluminescence can be considered rather complex as it is the contribution of three different signals, whose maxima occur at 2.28, 2.38 and 2.73 eV respectively.[12] DFT calculations attribute the luminescence of Zn_2GeO_4 to Zn 3d orbitals and the presence of native defects such as oxygen vacancies and zinc interstitials.[13,14] However, Zn_2GeO_4 nanoparticles emit different wavelengths depending on their morphology and particle size.[15] In particular, hexagonal

 doi:10.20944/preprints202309.0623.v1

microrods emit at 2.03, 2.40 and 2.86 eV,[16] nanowires at 1.89, 2.11 and 2.34 eV,[17] whilst small nanoparticles present luminescence signals at 2.4, 2.7 and 3.1 eV.[18] Therefore, such remarkable variations imply that morphology may affect Zn_2GeO_4 luminescence. Nevertheless, information about the optical properties of more types of undoped Zn_2GeO_4 particles is fairly limited. Covering a broader range of nanoparticle shapes and sizes may help to correlate the emitted light with different characteristic features of Zn_2GeO_4 crystallites with the ultimate goal of generating toxic-free nanophosphors with tunable properties.

Several studies have reported the preparation of Zn_2GeO_4 nanoparticles with a myriad of morphologies employing diverse synthetic methods. Solvothermal and hydrothermal procedures stand out among these methodologies due to the fine morphological and particle size control they provide. In particular, numerous articles report the solvothermal synthesis of Zn_2GeO_4 nanorods, commonly applied as photocatalysts,[19,20] for biosensing,[21] and for lithium batteries.[22,23] Apart from that, Zn_2GeO_4 ultrathin nanoribbons [24] can also be obtained following a hydrothermal method, while other procedures can be employed to prepare Zn_2GeO_4 with different morphologies: CVD (nanowires),[25–28] ceramic (polycrystals),[29] template-assisted method (hollow spheres),[30] etc.

In this article we report the reproducible hydrothermal synthesis of short Zn_2GeO_4 nanorods for light-emitting applications. An exhaustive structural, morphological and luminescence characterization was conducted, which allowed us to correlate the optoelectronic properties of this material with its morphological aspects, which is of maximum importance for its possible technological applications.

2. Materials and Methods

2.1. Synthesis

Zn_2GeO_4 nanoparticles were synthesized following a conventional hydrothermal method. The stoichiometric amounts GeO_2 (Sigma-Aldrich, 99.9%) were dissolved in a 0.33 M NaOH solution (Sigma-Aldrich, 98%) under continuous stirring. The corresponding amount of a $Zn(CH_3COO)_2{\cdot}2H_2O$ (Merck, 99.5%) solution was added dropwise and the resulting mixture was poured into a Teflon-line stainless steel autoclave. The autoclave was introduced in an oven for 12h at 100ºC. The as-obtained white precipitate was centrifuged, washed several times with water until pH = 7, and dried overnight. The synthesis was carried out several times to verify the reliability of the results obtained.

2.2. Structural characterization

X-ray diffraction (XRD) measurements were performed in a Bruker D8 ADVANCE A25 diffractometer using a Cu tube in Bragg-Brentano optics with fixed slits, Ni filter and a position sensitive LynxEye SSD160-2 detector. Patterns were recorded within the 2θ range of 5–80°, using a step size of 0.01° and a collection time of 1 s per step.

Transmission electron microscopy (TEM) experiments were conducted in a JEOL JEM 2100 microscope, located in the facilities of the National Center of Electron Microscopy (ICTS-CNME). The spatial resolution achieved operating at 200 kV in High Resolution Transmission Electron Microscopy mode (HRTEM) is 0.25 nm.

2.3. Photoluminescence measurements

A Horiba Jobin Ybon LabRaman Hr800 confocal microscope using a 325nm He-Cd laser as excitation source was used for photoluminescence (PL) measurements at room temperature (RT). An Edinburgh Instruments FLS1000 system, equipped with a 450W Xe lamp and a helium cryostat, was employed for acquiring photoluminescence-photoluminescence excitation (PL-PLE) spectra from 4K up to RT.

Preprints (www.preprints.org) | NOT PEER-REVIEWED | Posted: 11 September 2023 doi:10.20944/preprints202309.0623.v1

3. Results and discussion

3.1. Structural and morphological chacacterization

XRD was carried out in the as-synthesized nanoparticles, whose diffraction pattern is displayed in Figure 1. All the diffraction peaks were perfectly indexed on the rhombohedral space group R-3 basis of Zn_2GeO_4 (ICSD Collection Code: 68382), with cell parameters a = b = 14.28 Å and c =9.55 Å. This diffractogram clearly shows that nanocrystals possess a willemite-like structure[31] compared to the Zn_2GeO_4 reference, where the structure can be described as formed of tetrahedrally coordinated zinc and germanium atoms, sharing corners.[32] The absence of additional reflections, which could be attributed to impurities, is indicative of the remarkable purity of the Zn_2GeO_4 sample, even without the need for high-temperature thermal treatments. The relative wide maxima suggest the nanoparticle nature of the material.

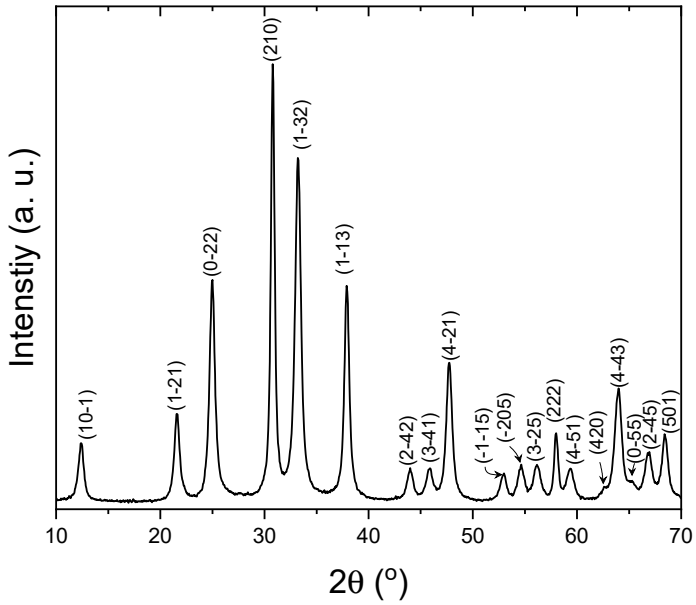

Figure 1. Indexed XRD pattern of the as-synthesized Zn_2GeO_4 nanoparticles.

The average crystal size has been calculated from the values of the form factor K, the wavelength of the incident radiation λ, the full width at half maximum B, of the diffraction maximum {210}, and the diffraction angle θ, along with Scherrer formula: $D = K \cdot \lambda / (B \cdot \cos\theta)$. The mean value is 17 ± 0.02 nm.

To confirm these results, transmission electron microscopy studies have been carried out. The low-magnification TEM image depicted in Figure 2a evidence that most nanoparticles possess a short rod-like morphology. Particle length and diameter distributions are presented in Figure 2b and c, revealing their small size. Specifically, particle length ranges between 24 and 54 nm with an average length of 37 ± 7 nm, whilst their mean diameter stands at 13 ± 3 nm, varying from 7 to 19 nm.

Preprints (www.preprints.org) | NOT PEER-REVIEWED | Posted: 11 September 2023 doi:10.20944/preprints202309.0623.v1

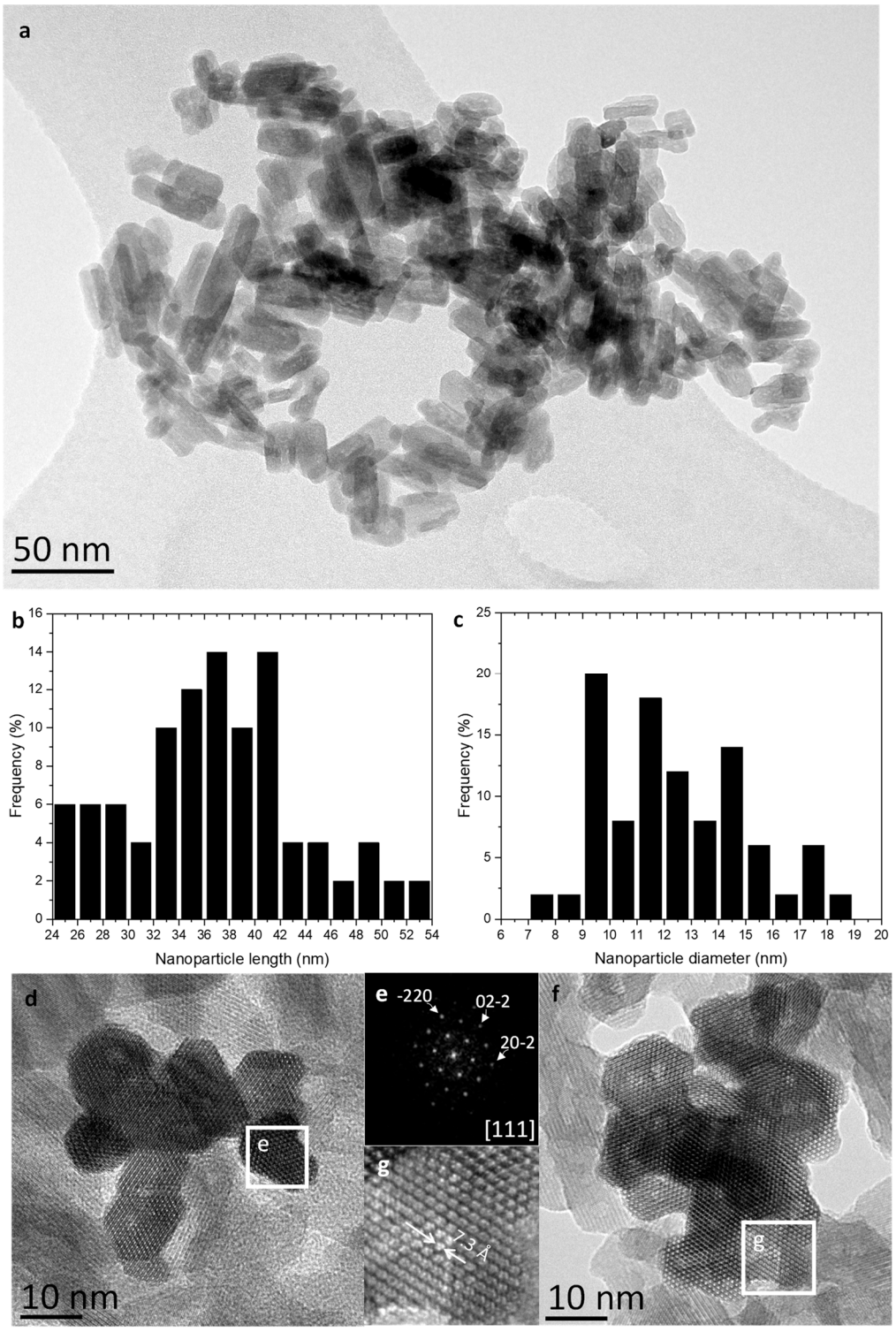

Figure 2. a) Representative low magnification TEM image of the as-synthesized Zn_2GeO_4 nanoparticles. b and c) Nanoparticle length and diameter distributions, respectively; d) HRTEM top-view image of a Zn_2GeO_4 nanoparticles agglomerate, from which a DDP was extracted (e). f) HRTEM top-view image of another Zn_2GeO_4 nanoparticles agglomerate, from which a magnified inset was extracted, (g), evidencing the presence of the characteristic tunnels of the willemite-type structure of Zn_2GeO_4.

In addition, the study by high-resolution electron microscopy (HRTEM) confirms the structure of the Zn_2GeO_4. Figures 2d and f depict the electron micrograph top-view images of representative agglomerates of Zn_2GeO_4 nanocrystals oriented along the [111] zone axis. As suggested by these

Preprints (www.preprints.org) | NOT PEER-REVIEWED | Posted: 11 September 2023 doi:10.20944/preprints202309.0623.v1

images, the radial morphology of these rod-like nanoparticles is greatly varied, but numerous cross-sections present 60º and 120º angles. Therefore, some of these nanoparticles may derive from distorted hexagonal and truncated triangular prismatic nanocrystals.

The digital diffraction pattern (DDP), extracted from one of the crystals (Figure 2e) clearly show the perfect willemite-like lattice of the nanocrystals. The reflections distances and angles measured are 3.6 Å at 60º, corresponding to {-220}, {02-2} and {20-2} planes oriented along a [111] zone axis. On the other hand, the characteristic tunnels, inherent to the willemite structure and parallel to the [111]-axis direction, can be readily discerned in Figure 2g, which depicts a magnified region from Figure 2f. The experimental diameter of the tunnels has been estimated using HRTEM images, and the measured values are approximately 7.3 Å, in accordance with the structure described for this oxide. [31]

3.2. Optical characterization of the nanoparticles

An in-depth study of the luminescence emission of the as-synthesized Zn_2GeO_4 nanoparticles was carried out. An analysis of the emission provides information about the electronic recombinations between conduction and valence bands or between the electronic levels caused by native defects within the bandgap. As a first step, room temperature luminescence of these Zn_2GeO_4 nanocrystals has been assessed. Figure 3 shows the room temperature luminescence spectrum acquired with an He-Cd laser (λ= 325 nm). A broad visible band covering practically the whole visible range is observed. PL spectra agree with the complex nature of the luminescence band involving several radiative centers. The broad luminescence emission can be deconvoluted intro three components (2.18 eV, 2.41 eV and 2.81 eV), as previously reported in other Zn_2GeO_4 nanoparticles growth by a different synthesis method.[18] The green-yellow broad band whose maximum is centered at 2.41 eV is the dominant contribution to the luminescence of this material. Li and co-workers [33] have suggested that this complex band is related to Ge centers (bands peaked at 2.18 eV and 2.41 eV) and oxygen defects (band peaked at 2.8 eV). These emission contributions are very close to the ones reported for microrods,[16] and rather distinct to Zn_2GeO_4 nanoparticles, nanowires and Zn_2GeO_4 in bulk form. [15,17,18] Hence, our results evidence that particles with similar morphologies, but clearly different particle sizes (nanorods and microrods) possess an analogous phosphor emission, which reinforces the relevant effect of morphology on the light emission efficiency of Zn_2GeO_4.

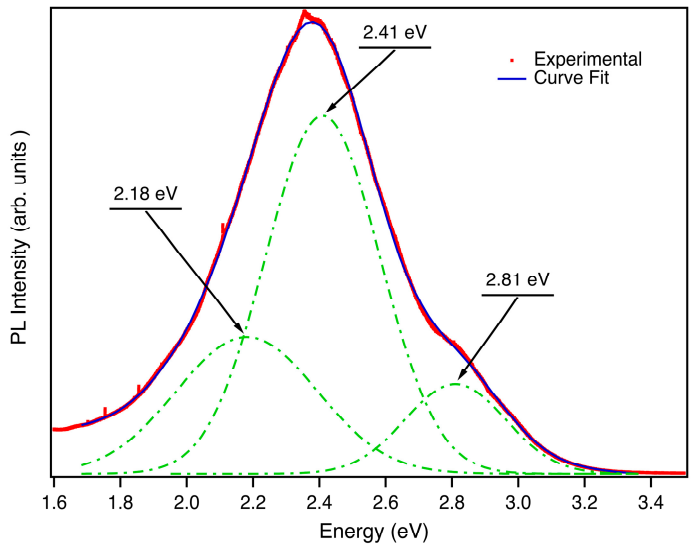

Figure 3. RT Luminescence spectra from Zn_2GeO_4 nanoparticles excited by an 325nm UV laser. Gaussian emission bands after deconvolution (dotted lines) are shown.

Preprints (www.preprints.org) | NOT PEER-REVIEWED | Posted: 11 September 2023 doi:10.20944/preprints202309.0623.v1

To understand better the origin of these emission bands, PL and PLE spectra were acquired at RT and at low temperature (4K). Figure 4 shows two PL-PLE maps: Figure 4a recorded at RT, and Figure 4b at 4K. In both cases, spectra were collected varying the excitation wavelength between 250-285 nm (4.96 – 4.35 eV) in order to ensure an excitation energy over, or close to the bandgap energy to be used, while the light emitted was recorded between 320-650 nm (3.88 – 1.9 eV).

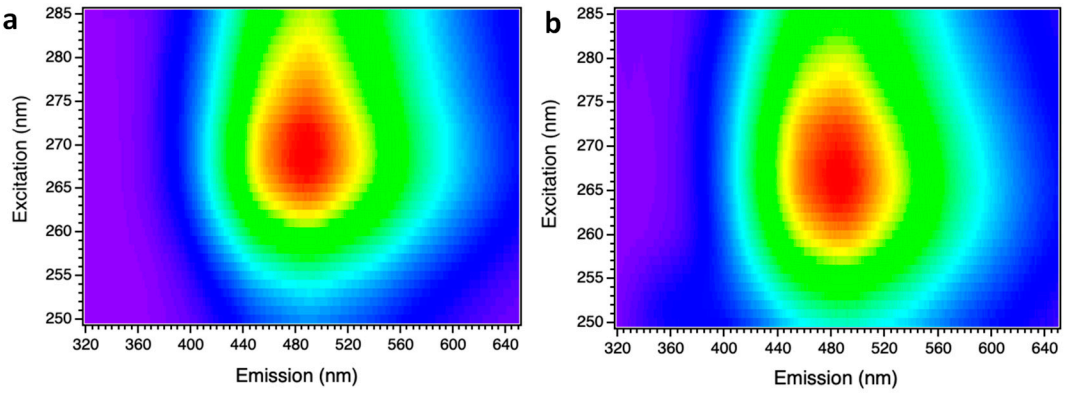

Figure 4. PL-PLE maps acquired on the nanoparticles (a) at RT and (b) at 4K. The color code employed for representing the relative PL-PLE intensity follows a rainbow-like trend: red corresponds to the highest normalized intensity, while violet pixels represent emission energies with the lowest relative intensities.

Analyzing the data from these emission maps, a broadening of the emission spectra occurs as temperature increases. Furthermore, it can be observed that the maximum emission of the sample occurs with an excitation in the range of 265-270 nm for 4K, and that this range increases to 260-280 nm when the sample is at RT. Using an excitation with an energy above the gap of the material produces an UV emission increase centered between 320 and 400 nm. Additionally, it is possible to observe how this emission decreases due to a reduction in the gap of the material when temperature rises.

Figure 5 shows emission spectra at RT and at 4K, acquired on the sample from 320 to 650 nm with an excitation wavelength of 250 nm in order to ensure an excitation energy over the bandgap energy.[18] At this excitation energy, a relatively intense emission centered at 3.4 eV is observed, which has been previously attributed to a recombination of V_O level electrons, acting as donor centers, with valence bands holes.[12] Therefore, the intensity of this band is directly related to oxygen vacancies. The broad feature observed in Figure 5a is not composed by a unique emission band as it is shown in Figure 5b. Deconvolution of the PL spectrum at 4K shows that it is composed of five gaussian emissions: three in the visible range (2.19 eV, 2.53 eV and 2.80 eV) and two gaussian emissions in the ultraviolet range (3.35 eV and 3.59 eV). The intensity evolution of the PLE spectrum of these two UV bands allows us to calculate the optical band gap of the nanoparticles.

Preprints (www.preprints.org) | NOT PEER-REVIEWED | Posted: 11 September 2023 doi:10.20944/preprints202309.0623.v1

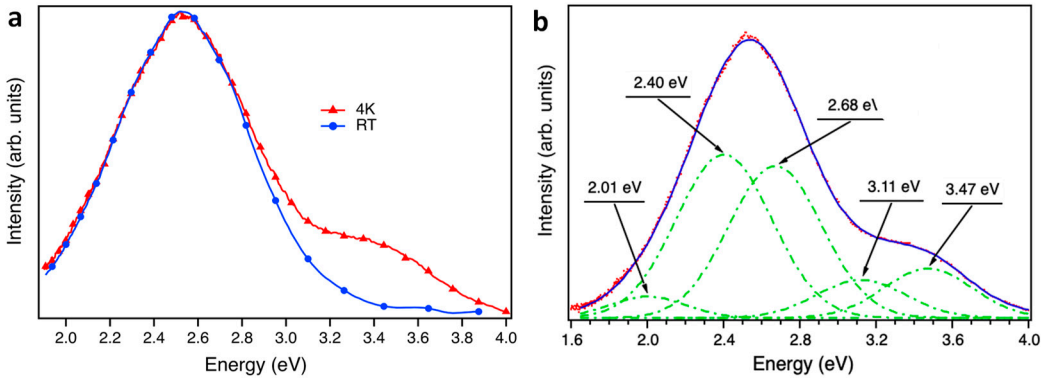

Figure 5. (a) Luminescence spectra, at 4K and RT, form nanoparticles under 250nm excitation wavelength of a Xenon lamp. (b)Gaussian emission bands after deconvolution (dotted lines) of the spectrum acquired at 4K are shown.

In that sense, Figure 6 shows the intensity emission of the nanoparticles at 360nm (3.44 eV) varying the excitation wavelength from 250 nm to 285 nm. The extrapolation of the sharp PLE decay at the shortest wavelengths to a linear function provides the value of the energy bandgap. The fitting linear curve of this extrapolation is plotted by the green discontinuous line the Figure 6. The calculated optical band gap of the nanoparticles is estimated at 4.75 eV at 4K, which is analogous to the reported for microwires (4.76 eV) and slightly larger than Zn_2GeO_4 long nanowires (4.68 eV).[34] Nevertheless, it greatly differs from the DFT-calculated bulk Zn_2GeO_4 (4.4 eV), and is smaller than the experimental Zn_2GeO_4 thin layers band gap (4.9 ± 0.1 eV).[35]

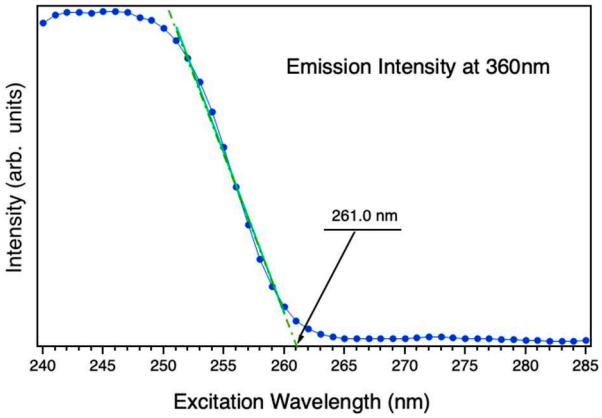

Figure 6. PLE spectrum at 4 K of the nanoparticles, in which the sharp decay is fitted to a linear function to calculate the energy of the bandgap.

These results clearly evidence the influence of crystallite morphology in the optoelectronic properties of Zn_2GeO_4 as nanoparticles with radically different external shapes present rather distinctive optoelectronic responses.

4. Conclusions

Zn_2GeO_4 short nanorods were successfully prepared by a reproducible hydrothermal synthesis. Nanoparticles are homogeneous in both particle size and morphology, with no impurities. PL spectra collected at both room temperature and at 4K are rather wide, covering almost all the visible range being centered in the green-yellow region. Spectra can be deconvoluted in several emission contributions, which are attributed to native vacancies. These contributions are comparable to the ones reported for Zn_2GeO_4 microrods, revealing the clear influence of Zn_2GeO_4 morphology on its luminescence. Zn_2GeO_4 nanorods bandgap was estimated (4.75 eV), which is similar to the one

obtained for microwires and nanowires, and clearly different from bulk Zn_2GeO_4. This strongly reinforces that morphology is a crucial parameter in the emission of Zn_2GeO_4. Further analyses will be performed to analyze oxygen and germanium vacancies in these nanorods to compare with other Zn_2GeO_4 morphologies with the aim to shed light onto their relationship with particle size and morphology, and their contribution to the variations in the as-observed Zn_2GeO_4 optoelectronic properties.

Author Contributions: MT and JRC: conceptualization; MT, JML and PH: methodology; MT and PH: formal analysis; MT and PH: investigation; MT and PH: writing – original draft preparation; MT, PH and JRC: writing – review and editing; JMGC and BM: supervision; JMGC and BM: funding acquisition. All authors have read and agreed to the published version of the manuscript.

Funding: This research was funded by Spanish Ministry of Science and Innovation through Research Projects PID 2020-113753RB-100 and PID2021-122562NB-I00.

Conflicts of Interest: Declare "The authors declare no conflict of interest.

References

1. Del Alamo, J.A. Nanometre-Scale Electronics with III-V Compound Semiconductors. *Nature* **2011**, *479*, 317–323.
2. Tanaka, A. Toxicity of Indium Arsenide, Gallium Arsenide, and Aluminium Gallium Arsenide. *Toxicol Appl Pharmacol* **2004**, *198*, 405–411.
3. Chitambar, C.R. Medical Applications and Toxicities of Gallium Compounds. *Int J Environ Res Public Health* **2010**, *7*, 2337–2361.
4. Leng, M.; Chen, Z.; Yang, Y.; Li, Z.; Zeng, K.; Li, K.; Niu, G.; He, Y.; Zhou, Q.; Tang, J. Lead-Free, Blue Emitting Bismuth Halide Perovskite Quantum Dots. *Angew Chem Int Ed* **2016**, *128*, 15236–15240.
5. Alfantazi, A.M.; Moskalyk, R.R. Processing of Indium: A Review. *Miner Eng* **2003**, *16*, 687–694.
6. European Comission *First Commission Interim Report on the Implementation of Pilot Projects and Preparatory Actions 2012*; 2012.
7. US Department of Energy *U.S. Department of Energy's Strategy to Support Domestic Critical Mineral to Support Domestic Critical Mineral and Material Supply Chain*; 2021.
8. Bavykin, D. V.; Friedrich, J.M.; Walsh, F.C. Protonated Titanates and TiO_2 Nanostructured Materials: Synthesis, Properties, and Applications. *Adv Mater* **2006**, *18*, 2807–2824.
9. Roy, P.; Berger, S.; Schmuki, P. TiO_2 Nanotubes: Synthesis and Applications. *Angew Chem Int Ed* **2011**, *50*, 2904–2939.
10. Ong, C.B.; Ng, L.Y.; Mohammad, A.W. A Review of ZnO Nanoparticles as Solar Photocatalysts: Synthesis, Mechanisms and Applications. *Renew Sust Energ Rev* **2018**, *81*, 536–551.
11. Wang, Z.L. Zinc Oxide Nanostructures: Growth, Properties and Applications. *J Phys - Condensed Matter* **2004**, *16*, R829.
12. Liu, Z.; Jing, X.; Wang, L. Luminescence of Native Defects in Zn_2GeO_4. *J Electrochem Soc* **2007**, *154*, H500.
13. Xie, Z.Y.; Lu, H.L.; Zhang, Y.; Sun, Q.Q.; Zhou, P.; Ding, S.J.; Zhang, D.W. The Electronic Structures and Optical Properties of Zn_2GeO_4 with Native Defects. *J Alloys Compd* **2015**, *619*, 368–371.
14. Dolado, J.; Martínez-Casado R.; Hidalgo P.; Gutierrez R.; Dianat A.; Cuniberti G.; Domínguez-Adame F.; Díaz E.; Méndez B. Understanding the UV luminescence of zinc germanate: The role of native defects. *Acta Mater* **2020,** *196,* 626-634.
15. Duan, X.; Yuan, M.; Ou, K.; Zhao, W.; Tian, T.; Duan, W.; Zhang, X.; Yi, L. Controlled Preparation of Undoped Zn_2GeO_4 Microcrystal and the Luminescent Properties Resulted from the Inner Defects. *Mater Today Commun* **2021**, *27*, 102359.
16. Hidalgo, P.; López, A.; Méndez, B.; Piqueras, J. Synthesis and Optical Properties of Zn_2GeO_4 Microrods. *Acta Mater* **2016**, *104*, 84–90.
17. Xu, J.; Wang, C.; Zhang, Y.; Liu, X.; Liu, X.; Huang, S.; Chen, X. Structural, Vibrational and Luminescence Properties of Longitudinal Twinning Zn_2GeO_4 Nanowires. *CrystEngComm* **2013**, *15*, 764–768.
18. Dolado, J.; García-Fernández, J.; Hidalgo, P.; González-Calbet, J.; Ramírez-Castellanos, J.; Méndez, B. Intense Cold-White Emission Due to Native Defects in Zn_2GeO_4 Nanocrystals. *J Alloys Compd* **2022**, *898*, 162993..
19. Liu, Q.; Low, Z.X.; Li, L.; Razmjou, A.; Wang, K.; Yao, J.; Wang, H. ZIF-8/ Zn_2GeO_4 Nanorods with an Enhanced CO_2 Adsorption Property in an Aqueous Medium for Photocatalytic Synthesis of Liquid Fuel. *J Mater Chem A Mater* **2013**, *1*, 11563–11569.
20. Huang, J.; Ding, K.; Hou, Y.; Wang, X.; Fu, X. Synthesis and Photocatalytic Activity of Zn_2GeO_4 Nanorods for the Degradation of Organic Pollutants in Water. *ChemSusChem* **2008**, *1*, 1011–1019.

21. Wang, J.; Ma, Q.; Zheng, W.; Liu, H.; Yin, C.; Wang, F.; Chen, X.; Yuan, Q.; Tan, W. One-Dimensional Luminous Nanorods Featuring Tunable Persistent Luminescence for Autofluorescence-Free Biosensing. *ACS Nano* **2017**, *11*, 8185–8191.
22. Feng, J.K.; Lai, M.O.; Lu, L. Zn_2GeO_4 Nanorods Synthesized by Low-Temperature Hydrothermal Growth for High-Capacity Anode of Lithium Battery. *Electrochem Commun* **2011**, *13*, 287–289.
23. Lim, Y.R.; Jung, C.S.; Im, H.S.; Park, K.; Park, J.; Cho, W. Il; Cha, E.H. Zn_2GeO_4 and Zn_2SnO_4 Nanowires for High-Capacity Lithium- and Sodium-Ion Batteries. *J Mater Chem A Mater* **2016**, *4*, 10691–10699.
24. Liu, Q.; Zhou, Y.; Kou, J.; Chen, X.; Tian, Z.; Gao, J.; Yan, S.; Zou, Z. High-Yield Synthesis of Ultralong and Ultrathin Zn_2GeO_4 Nanoribbons toward Improved Photocatalytic Reduction of CO_2 into Renewable Hydrocarbon Fuel. *J Am Chem Soc* **2010**, *132*, 14385–14387.
25. Zhou, X.; Zhang, Q.; Gan, L.; Li, X.; Li, H.; Zhang, Y.; Golberg, D.; Zhai, T. High - Performance Solar-Blind Deep Ultraviolet Photodetector Based on Individual Single-Crystalline Zn_2GeO_4 Nanowire. *Adv Funct Mater* **2016**, *26*, 704–712.
26. Yan, C.; Lee, P.S. Synthesis and Structure Characterization of Ternary Zn_2GeO_4 Nanowires by Chemical Vapor Transport. *J Phys Chem C* **2009**, *113*, 14135–14139.
27. Gu, Z.; Liu, F.; Li, X.; Pan, Z.W. Luminescent Zn_2GeO_4 Nanorod Arrays and Nanowires. *Phys Chem Chem Phys* **2013**, *15*, 7488–7493.
28. Liu Z.; Huang H.; Liang B.; Wang X.; Wang Z.; Chen D.; Shen G. Zn_2GeO_4 and and In_2Ge2O_7 Nanowire Mats Based Ultraviolet Photodetectors on Rigid and Flexible Substrates. *Opt Express* **2012**, *20*, 2982–2991.
29. Chi, F.; Wei, X.; Jiang, B.; Chen, Y.; Duan, C.; Yin, M. Luminescence Properties and the Thermal Quenching Mechanism of Mn2+ Doped Zn_2GeO_4 Long Persistent Phosphors. *Dalton T* **2018**, *47*, 1303–1311.
30. Liu, J.; Zhang, G.; Yu, J.C.; Guo, Y. In Situ Synthesis of Zn_2GeO_4 Hollow Spheres and Their Enhanced Photocatalytic Activity for the Degradation of Antibiotic Metronidazole. *Dalton T* **2013**, *42*, 5092–5099.
31. Breternitz, J.; Fritsch, D.; Franz, A.; Schorr, S. A Thorough Investigation of the Crystal Structure of Willemite-Type Zn_2GeO_4. *Z Anorg Allg Chem* **2021**, *647*, 2195–2200.
32. Klaska, K.-H.; Eck, J.C.; Pohl, D. New Investigation of Willemite. *Acta Cryst*. **1978**, 34, 3324-3325.
33. Li L.; Su Y.; Chen Y.; Gao M.; Chen Q.; Feng Y. Syntesis and Photoluminiescence Properties of Hierarchical Zinc Germanate Nanoestructures. *J Comput Theor Nanosci* **2010**, *3*, 1–5.
34. Yan, C.; Singh, N.; Lee, P.S. Wide-Bandgap Zn_2GeO_4 Nanowire Networks as Efficient Ultraviolet Photodetectors with Fast Response and Recovery Time. *Appl Phys Lett* **2010**, *96*, 053108.
35. Luo, S.; Trefflich, L.; Selle, S.; Hildebrandt, R.; Krüger, E.; Lange, S.; Yu, J.; Sturm, C.; Lorenz, M.; Wenckstern, H. Von; et al. Ultrawide Bandgap Willemite-Type Zn_2GeO_4 epitaxial Thin Films. *Appl Phys Lett* **2023**, *122*, 031601.